


## Article

# Electrochemical Characteristics and Corrosion Mechanisms of High-Strength Corrosion-Resistant Steel Reinforcement under Simulated Service Conditions

Jing Yuan <sup>1,2</sup>, Pei Li <sup>3</sup>, Huanhuan Zhang <sup>1</sup>, Shubiao Yin <sup>1,\*</sup>  and Mingli Xu <sup>1</sup>

<sup>1</sup> College of Metallurgy and Energy Engineering, Kunming University of Science and Technology, Kunming 650032, China; lgcyj@xinsteel.com.cn (J.Y.); zhanghuanhuan@stu.kust.edu.cn (H.Z.); xumingli0326@126.com (M.X.)

<sup>2</sup> Xinyu Iron & Steel Group Co., Ltd., Xinyu 338001, China

<sup>3</sup> Institute for Carbon Neutrality, University of Science and Technology Beijing, Beijing 100083, China; lp1277504201@163.com

\* Correspondence: yinshubiao@kust.edu.cn

**Abstract:** Long-term steel reinforcement corrosion greatly impacts reinforced concrete structures, particularly in marine and coastal settings. Concrete failure leads to human casualties, requiring extensive demolition and maintenance, which represents an inefficient use of energy and resources. This study utilizes microscopic observation, atomic force microscopy (SKPM), electrochemical experiments, and XPS analysis to investigate the corrosion behavior of 500CE and 500E under identical conditions. We compared 500E with 500CE, supplemented with 0.94% Cr, 0.46% Mo, 0.37% Ni, and 0.51% Cu through alloying element regulation to obtain a finer ferrite grain and lower pearlitic content. The results indicate that 500CE maintains a stable potential, whereas 500E exhibits larger grain sizes and significant surface potential fluctuations, which may predispose it to corrosion. In addition, despite its more uniform microstructure and stable electrochemical activity, 500E shows inferior corrosion resistance under prolonged exposure. The electrochemical corrosion rate of 500CE in both the pristine and passivated states and for various passivation durations is slower than that of 500E, indicating superior corrosion performance. Notably, there is a significant increase in the corrosion rate of 500E after 144 h of exposure. This study provides valuable insights into the chloride corrosion phenomena of low-alloy corrosion-resistant steel reinforcement in service, potentially enhancing the longevity of reinforced concrete structures.

**Keywords:** chloride corrosion; alkaline passivation; operational status; corrosion resistance



**Citation:** Yuan, J.; Li, P.; Zhang, H.; Yin, S.; Xu, M. Electrochemical Characteristics and Corrosion Mechanisms of High-Strength Corrosion-Resistant Steel Reinforcement under Simulated Service Conditions. *Metals* **2024**, *14*, 876. <https://doi.org/10.3390/met14080876>

Academic Editor: Youngsik Kim

Received: 26 June 2024

Revised: 15 July 2024

Accepted: 24 July 2024

Published: 30 July 2024



**Copyright:** © 2024 by the authors. Licensee MDPI, Basel, Switzerland. This article is an open access article distributed under the terms and conditions of the Creative Commons Attribution (CC BY) license (<https://creativecommons.org/licenses/by/4.0/>).

## 1. Introduction

Statistical data and research findings indicate that long-term corrosion of steel reinforcement significantly impacts the durability of reinforced concrete structures. In marine engineering and coastal construction, the rusting of steel, a direct consequence of corrosion, is identified as the predominant cause of structural failure [1]. The failure of concrete structures and the premature cessation of service not only result in human casualties but also necessitate extensive demolition and maintenance activities, leading to inefficient use of energy and resources [2–5]. In various industrial sectors, the corrosion of steel materials poses a substantial threat to the environment [6,7]. For instance, leaks from corroded pipelines and storage tanks in the chemical industry directly contribute to atmospheric pollution. As human industry rapidly advances, it poses new challenges to the service life of reinforced concrete structures, particularly those deployed in harsh and challenging environments [8]. The development of cost-effective, high-strength, low-alloy corrosion-resistant steel reinforcement and a comprehensive understanding of its corrosion mechanisms is crucial for the sustainable utilization of marine resources and the

prudent management of engineering resources [9]. In recent years, significant progress has been made in the field of corrosion-resistant reinforcing bars. First, the development of high-performance corrosion-resistant coatings has significantly improved the durability of steel bars. The application of self-repairing coatings and nano-coatings can automatically repair the coating when it is damaged and form a stronger protective film, thus effectively blocking the erosion of chlorides. Second, breakthroughs have also been made in modified concrete technology, with the use of high silicate cement and conductive concrete enhancing the protection of concrete against steel reinforcement and reducing the risk of chloride penetration. In addition, the research progress of new reinforcing steel materials should not be ignored. Stainless steel rebar and carbon fiber composite rebar are becoming the preferred materials for highly corrosive environments due to their excellent corrosion resistance. The introduction of intelligent monitoring technology, especially steel reinforcement and intelligent concrete integrated with corrosion sensors, provides real-time monitoring and early warning functions, which enhance our grasp of the corrosion status. Finally, the application of green technologies, such as low-carbon steel reinforcement and environmentally friendly anticorrosion agents, not only reduces the environmental impact of the production process but also improves the corrosion resistance of materials to a certain extent. In general, these research results and technological advances have contributed to continuous innovation in the field of corrosion-resistant reinforcing bars, improving the durability and safety of building structures [6,10–13].

Currently, abundant research worldwide indicates that rebar corrosion poses a significant challenge to construction projects globally. In numerous coastal countries across Europe, America, Japan, Korea, and Australia, chloride-induced corrosion stands out as the primary cause of premature structural failure and early attainment of service life limits in building engineering [10,14–18]. The penetration of chloride ions through concrete protective layers into the surface of reinforcing bars, crystallizing on their surface and initiating localized corrosion, eventually transitions to uniform corrosion and determines the lifespan of concrete structures [19,20]. Therefore, enhancing the service life of reinforced concrete structures in chloride environments hinges on impairing the corrosive intensity of chlorides and improving the corrosion resistance of the rebar itself [3,21].

Historically, methods to mitigate chloride-induced corrosion have primarily focused on the concrete itself. They utilize inhibitors to hinder chloride ingress and reduce chloride accumulation within concrete environments, thereby improving the surface conditions for reinforcing bars [4,22]. When boats are used in the marine environment, the following measures can be taken to prevent chlorides from attacking hull metals: first, the hull is thoroughly cleaned using water and detergents to remove salt and dirt from the surface; next, a rust inhibitor designed for the marine environment, such as an anti-corrosion coating containing zinc, is applied, which forms a protective film on the metal surface and acts as a sacrificial anode to prevent chloride penetration; finally, the coatings are regularly inspected and maintained to ensure that they are in good condition, and any peeling or damage to the coating should be replaced in a timely manner in order to maintain effectively anticorrosion protection of the hull. While initially effective at substantially reducing  $\text{Cl}^-$  diffusion rates and delaying rebar corrosion processes, these methods resulted in a significant increase in construction burdens [23,24]. Moreover, they overlooked material defects such as cracks and voids in hardened concrete, which ultimately failed to address chloride diffusion corrosion issues during later stages of service life [25].

In addition to slowing the process of chloride ion ingress to the rebar surface, methods such as application of protective coatings and cathodic protection on the rebar surface are frequently implemented [11,12,26]. Protective coatings, for instance, involve electrostatically spraying a thin layer of epoxy resin onto the rebar surface. Epoxy resin, renowned for its compactness and excellent protective properties, effectively separates the rebar substrate from corrosive media such as chlorides. Epoxy coatings are commonly used as a protective layer on the surface of steel bars to significantly enhance their corrosion resistance. Common types of epoxies include standard epoxy coatings, epoxy-polyurethane

composite coatings, and epoxy powder coatings. Standard epoxy coatings are widely used in reinforcing steel surfaces due to their excellent adhesion and corrosion resistance and their ability to effectively block chlorides and moisture. Epoxy–urethane composite coatings combine the benefits of epoxy and polyurethane to provide enhanced weathering and chemical resistance. Epoxy powder coatings are also used in rebar protection due to their solvent-free properties and ability to provide uniform coverage. These epoxy coatings are widely used in bridges, roads, and building structures, obviously extending the service life of reinforcing steel and improving the durability of the structure. The application of epoxy-resin-coated rebar became widespread in the construction industry starting from the 1990s [27].

Apart from utilizing epoxy resin coatings to impede  $\text{Cl}^-$  permeation and enhance the corrosion resistance of steel rebars, stainless-steel-clad rebars have been developed domestically and internationally [28]. This technology involves encapsulating a layer of stainless steel onto the surface of ordinary rebars, thereby combining the corrosion resistance properties of stainless steel with relatively lower production costs. Currently, there are two primary methods for stainless steel clad rebars. One method involves processing stainless steel into tubular forms, filling them with carbon steel particles, and subsequently rolling them into rebars [29–31]. The other method involves spraying a stainless steel protective layer onto casting blanks, which are then rolled into rebars [32]. These methods share several characteristics: First, they form a protective layer with excellent corrosion resistance due to the stainless steel cladding. Second, they incur relatively higher production and processing costs compared to ordinary rebars due to the use of costly stainless steel. Additionally, due to the rolling process, the uniformity of the stainless steel shell cannot be guaranteed completely, and it is susceptible to separation from the steel core under the influence of rolling temperatures and heat treatment processes, resulting in differences in yield strength [7,33]. Lastly, in engineering applications, welding presents challenges, and improper weld joint practices may lead to corrosion of the steel core. Furthermore, their application is relatively limited, and there are fewer manufacturers in the industry [27]. This study focuses on 500 Mpa grade low-alloy corrosion-resistant rebars, which are noted for exceptional corrosion resistance and modest production costs in service environments. The 500CE and 500E grades, discussed in the paper, are hot rolled ribbed steel bars with yield strength of not less than 500 MPa, with specifications of 12 mm–32 mm, which are mainly used in reinforced concrete structures with good seismic performance. They are well-suited to meeting the requirements of the majority buildings. The fundamental reason for rebar corrosion in chloride environments lies in its inherent sensitivity to chloride ions and the high concentration of the corrosive media. Conventional low-alloy corrosion-resistant rebars of standard strength have matured in production and practical applications, including deployment in actual service environments. Generally, the most economical way to improve the corrosion resistance of low-alloyed steels is microalloying the steel with elements, such as Cu, Cr, Ni, and P. Therefore, several researchers have committed to investigating the effect of microalloying on the corrosion behavior of low-alloyed steels [34].

This study differs from previous ones that focus solely on corrosion behavior in a single chloride salt environment. Instead, it integrates the specific characteristics of the environment where the rebar is utilized. In addition, the corrosion behavior of the rebar is carried out in the simulation of its corrosion at different time durations after its prolonged passivation in the concrete. Moreover, the results are compared with the direct corrosion behavior of chloride salts. However, there is a need to analyze and study the early- and later-stage corrosion behaviors of high-strength corrosion-resistant rebars in chloride environments, as well as their electrochemical characteristics under service conditions. This research aims to provide a scientific theoretical basis for the application of high-strength corrosion-resistant rebars in marine engineering.

## 2. Materials and Methods

A 12 mm diameter 500 MPa grade low-alloy seismic corrosion-resistant steel rebar (designated as 500CE) was chosen for the experimental material. For comparative purposes, high-strength seismic steel bars (designated as 500E) without alloying elements were used. From a chemical composition point of view, four corrosion-resistant alloying elements are added to 500CE, and their contents are controlled at a low level to control the cost, and no other alloying components are additionally added to 500E. The 500CE steel reinforcement exhibits a yield strength  $\geq 500$  MPa, tensile strength  $\geq 620$  MPa, a strength-to-yield ratio  $\geq 1.5$ , fracture elongation  $\geq 15\%$ , and total elongation under maximum load  $\geq 8\%$ . Their chemical compositions are presented in Table 1.

**Table 1.** Chemical composition of 500CE and 500E steels (wt.%).

No.	Chemical Composition									
	C	Si	Mn	S	P	Cr	Mo	Ni	Cu	Fe
500CE	0.012	0.50	1.12	$\leq 0.004$	$\leq 0.018$	0.94	0.46	0.37	0.51	Bal
500E	0.013	0.70	1.52	$\leq 0.008$	$\leq 0.025$	-	-	-	-	Bal

The microstructural analysis is conducted using an electron metallographic microscope (LEICA Co., Wetzlar, Germany) to photograph the microstructures of two types of steel reinforcements. Prior to imaging, the steel reinforcements undergo a rigorous preprocessing procedure. First, an electrical discharge machine process, which is programmed through a control panel to cut metallographic samples with a thickness of 10 mm, is undertaken for both types of reinforcements. The electrical discharge process does not generate excess heat, thus preserving the original structure of the reinforcements. After cutting (WENJIE Co., Suzhou, China), the samples are meticulously dry-ground using sandpaper ranging from 180 to 800 grit, followed by successive wet grinding with sandpapers ranging from 1000 to 5000 grit to eliminate any visible surface scratches. Following pre-grinding, a metallographic polishing machine is utilized for further refinement. Prior to polishing, a layer of alumina polishing compound is sprayed onto a damp polishing cloth for 10–15 s, ensuring complete coverage and uniformity. Polishing is then carried out along the direction perpendicular to the 5000 grit scratches until the experimental surface achieves a flawless mirror finish.

Initially, the steel samples are machined from rod-shaped to standardized 10 mm  $\times$  10 mm  $\times$  3 mm dimensions using an electrical discharge machine. Subsequently, one side of each specimen is meticulously welded to a single-core copper wire using a soldering iron and solder. The opposite side undergoes sequential dry grinding with 180-to-800 grit sandpaper, followed by wet grinding with 1000-to-5000 grit sandpaper to eliminate visible scratches. Polishing proceeds until the working surface achieves a mirror-like finish devoid of imperfections. Following surface preparation, non-working areas are encapsulated using molten wax, meticulously preserving the polished test surfaces exposed for subsequent electrochemical evaluation or other treatments such as passivation and corrosion testing.

The electrolytic cell employs a 2 wt% NaCl (mass fraction) solution as the electrolyte. The electrochemical specimens are specified as 10 mm  $\times$  10 mm  $\times$  3 mm, with a working test area of 100 mm<sup>2</sup>. The processing sequence involves electrical discharge machining, copper core wire welding, specimen surface preparation, and encapsulation. Electrochemical corrosion testing was conducted using the CHI660E electrochemical workstation (CHENHUA Co., Shanghai, China), with a 2 wt.% NaCl solution employed as the corrosive medium. The reason for using 2 wt.% NaCl solution in the paper is to follow the experimental solution stipulated in the Chinese industry standard “YB/T4367-2014 Corrosion Test Method for Steel Reinforcing Bars in Chloride-Ionized Environments” due to the low content of alloy additions to the applicable reinforcing bars under the standard and the fact that the applicable environments are generally concrete or environments that do not come into contact with seawater (3.5 wt.% NaCl) directly. Therefore, the standard

specifies that the test solution is 2 wt.% NaCl. The sample electrode was set as the working electrode, a saturated calomel electrode served as the reference electrode, and a platinum sheet electrode acted as the auxiliary electrode. The corrosion area was defined as a circular surface with a diameter of 12 mm, and the test temperature was maintained at 25 °C. Tafel polarization tests were performed at a scan rate of 0.01 V/s, ranging from 1.5 V to −1.5 V, and EIS tests were conducted over a frequency range of 0.01 Hz to 10 kHz. As Figure 1 shows,  $R_s$  represents the solution resistance between the working electrode in the electrolyte cell and the saturated calomel electrode,  $Q_f$  denotes the constant phase element of the double-layer capacitance,  $R_f$  corresponds to the transfer resistance of the film layer,  $Q_{dl}$  signifies the capacitance of the surface film on the substrate, and  $R_{ct}$  denotes the resistance of the film layer.

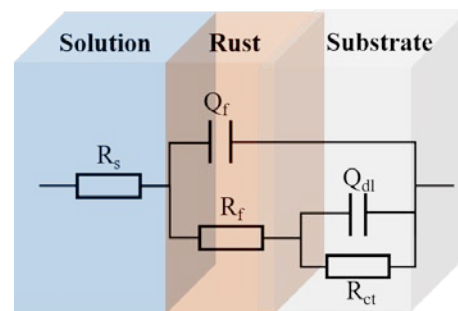


**Figure 1.** EIS equivalent circuit models.

Following these procedures, the samples are subjected to open circuit potential (OCP) measurements, alternating current impedance spectroscopy, and polarization curve analysis. OCP measurements capture the electrode potential in the absence of external current after an equilibration period of 1800 s. Alternating current impedance spectroscopy applies small-amplitude sine wave signals to the electrode, evaluating the electrolyte's response across various frequencies to characterize the electrochemical impedance, followed by data analysis to determine parameters such as the corrosion potential ( $E_{corr}$ ) and corrosion current density ( $I_{corr}$ ) of the steel reinforcement. The SKPFM measurements were conducted using the Jupiter XR system (OXFORD CO., New York, NY, USA) with the AC air mode. The scan rate was set to 2.0 Hz, the setpoint value was 400.00 mV, and the integral gain was set to 50. SKPFM samples are mainly prepared in the following way: the specimen to be tested will be cut into a 10 mm × 10 mm × 1 mm cube; the surface will be tested in accordance with the metallographic specimen preparation process for the preparation of the use of sandpaper for sanding and polishing, alongside the use of 4 wt.% nitric acid–alcohol microstructure corrosion; and the sample table contact surface will be ground and polished to flat to ensure conductivity. The chemical states of the layer surface were tested with AXIS ULTRA<sup>DL</sup> (XPS) (Kratos Co., Tokyo, Japan). The XPS samples were mainly selected to detect the surface rust powder after corrosion for different durations. Immediately after the corrosion was completed, the surface rust powder, approximately 1–2 g, was collected using a spatula and stored under vacuum conditions. The sample surface must be clean and homogeneous. The sample needs to be cleaned or treated to remove surface contaminants. We placed the sample in the sample chamber of the XPS instrument. Measurements need to be performed under high vacuum conditions (typically  $10^{-7}$  to  $10^{-9}$  Torr) to avoid photoelectron loss or scattering in the air. An X-ray light source (Al K $\alpha$  line) was used to excite the photoelectrons on the sample surface. (The X-ray wavelength used was 1486.6 eV). When X-rays excite the sample, photoelectrons are released from the sample surface. The energy of the photoelectrons is related to the chemical environment in which they are released, and through measuring the kinetic energy of the photoelectrons, their binding energy can be determined. For passivation, a saturated Ca(OH)<sub>2</sub> solution is applied, with a treatment duration of 60 days. Post-passivation, electrochemical assessments are conducted.

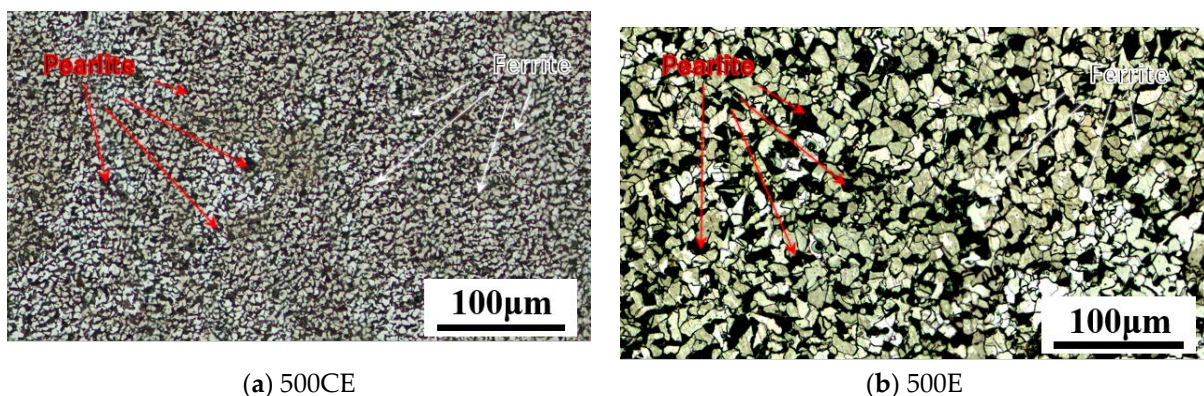
Subsequently, the specimens undergo controlled-temperature chloride corrosion in 2 wt.% NaCl (mass fraction) solution for durations ranging from 1 to 576 h.

### 3. Results and Analysis

#### 3.1. Microstructure

Based on the metallographic structure analysis, the 500CE steel exhibits a predominantly pearlite–ferrite microstructure with a uniform distribution. The smelting process effectively controls the carbon content, thus minimizing carbide formation in the final steel reinforcement product.

Conversely, the microstructure of 500E steel reveals a pearlite–ferrite matrix with higher carbon content. This microstructure is presented in Figure 2. Regularly shaped carbide phases are observed to be adjacent to the pearlite grains, which detrimentally impacts their corrosion resistance properties. Statistically, the average size of 500CE ferrite grains is 6.45  $\mu\text{m}$ , the maximum grain size is 20.39  $\mu\text{m}$ , and the minimum grain size is 1.31  $\mu\text{m}$ . 500E grains have an average size of 10.26  $\mu\text{m}$ , a maximum grain size is 27.19  $\mu\text{m}$ , and a minimum grain size is 1.32  $\mu\text{m}$ . To enhance corrosion resistance, 500CE steel has a lower carbon content. Furthermore, to maintain structural strength, it incorporates specific amounts of Cr, Mo, Ni, and Cu as corrosion-resistant additives. These elements help to reduce its susceptibility to corrosion over its operational lifespan.



(a) 500CE

(b) 500E

**Figure 2.** The microstructure of corrosion-resistant steel reinforcement compared to conventional steel reinforcement: (a) 500CE; (b) 500E.

#### 3.2. Microstructure SKPM Test

The microstructure morphology and the potential variation between selected regions are shown in Figure 3a–h for the two types of steel. First of all, before conducting tests on the original microstructure of the two types of steel bars, the samples undergo grinding and polishing. Additionally, nitric acid–alcohol corrosion is applied to reveal the microstructure. The table illustrates the potential measurements relative to the tip of an atomic force microscope (AFM) probe. The equipment is set to apply a constant voltage of 3 V to the probe tip. This process detects the surface potential of the sample, thereby obtaining the potential of the sample’s microstructure. Due to human processing errors in the sample preparation process, we cannot directly judge the influence of its surface potential distribution on the corrosion resistance through the measured potential; thus, we only consider the relative potential changes within the marked range of the measured tissues and the influence of inter-tissue potential differences on the corrosion resistance from the potential distribution and change trend. Table 2 provides information on the relative potentials within the selected regions (relative to the probe) and the potential differences between different phases. Through height retrace and 3D images, it is observed that the metallographic microstructure of 500CE and 500E after nitric acid–alcohol corrosion exhibits a consistency with what is observed under optical microscopy. Under the same corrosion conditions, the maximum relative depth of corrosion on the surface microstructure reaches

700 nm for 500CE and 415 nm for 500E. In the potential data, we can see that the alloying elements under the regulation of the 500CE microstructure’s ferrite grains are finer, and their interorganizational potential is always in the negative potential; while for 500E potential fluctuations, due to the reasons for the size of the grains, there are positive and negative potential fluctuations on the surface of the organization; it is more sensitive to potential fluctuations, and this may induce serious corrosion under extreme potential difference. The former, controlled by alloying elements, shows finer ferrite grain size and a much lower proportion of pearlite compared to the latter. This ensures uniform corrosion progression during the corrosion process, preventing catastrophic corrosion failure.

Table 2. Raw and fitted data on the potential distribution of samples in selected areas.

Sample	Probe Potential/V	Raw Data/V			Fitted Data/V		
		Max	Min	$\Delta E$	Max	Min	$\Delta E$
500CE	3.00	+0.006	−0.185	0.191	−0.054	−0.103	0.049
500E		+0.044	−0.036	0.080	0.024	−0.021	0.045

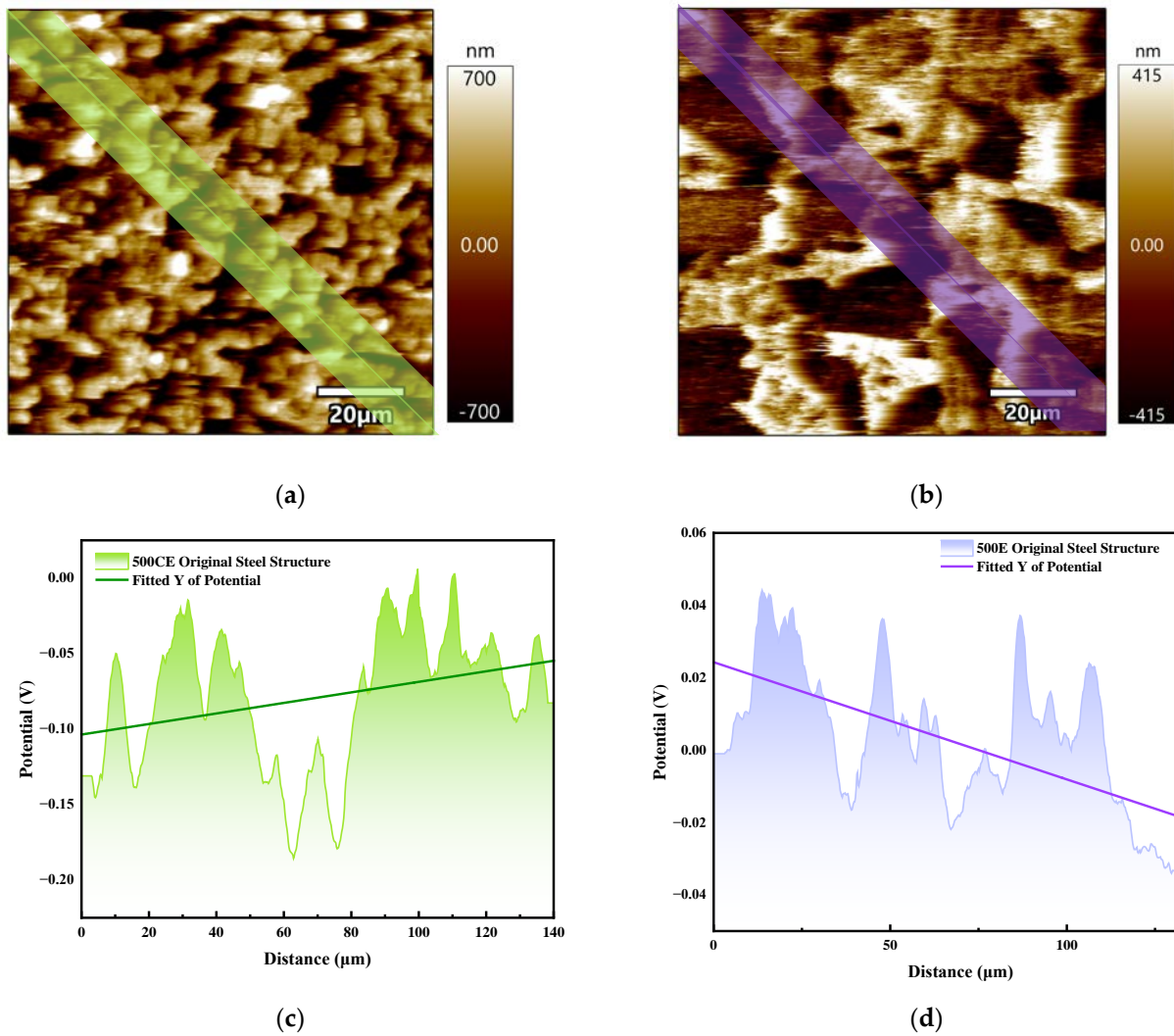
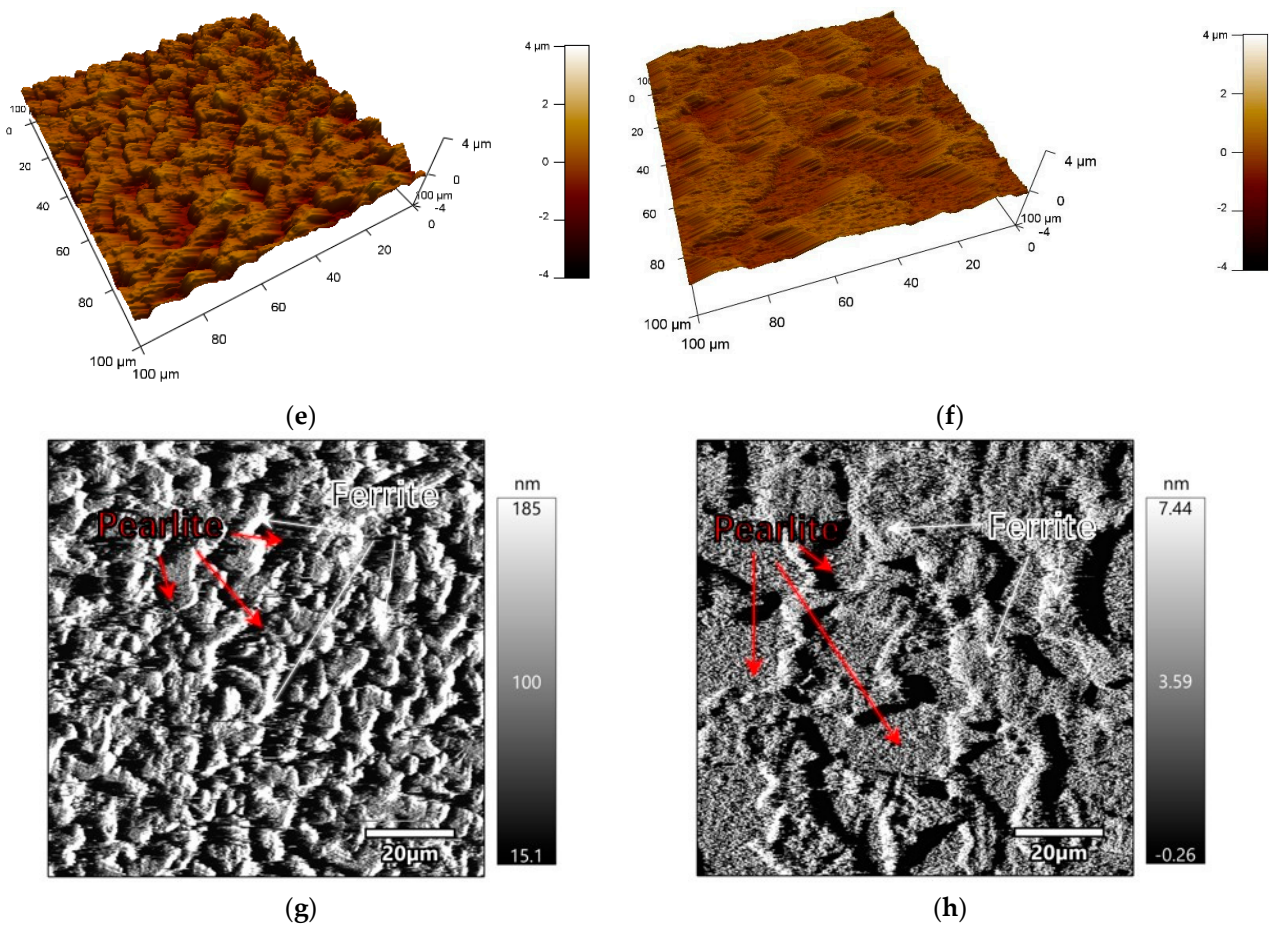


Figure 3. Cont.



**Figure 3.** Atomic force microscopy height maps and three-dimensional morphology of experimental steel reinforcement microstructures, along with local potential variations in corresponding regions: (a) 500CE height retrace; (b) 500E height retrace; (c) 500CE potential distribution; (d) 500E potential distribution; (e) 500CE microstructure 3D morphology; (f) 500E microstructure 3D morphology; (g) 500CE amplitude retrace; (h) 500E amplitude retrace.

### 3.3. Electrochemical Corrosion Performance Analysis

Figure 3 shows the Tafel curves (a), Nyquist plots (b), and Bode plots (c) of the samples in the original, passivated, and passivated corroded states of 500CE and 500E in 2wt.% NaCl saline solution at stable open circuit potential. Additionally, Table 3 indicates that in their original states, 500CE exhibits superior corrosion resistance to 500E, which is primarily reflected in its more positive open circuit potential and comparable corrosion current density, with similar trends observed in both the anodic and cathodic regions of the plots.

In the chloride environment, passivation is observed in the anodic region of 500CE's original state, characterized by regions of anodic dissolution and passivation breakdown ( $E_{pit}$ ). Breakdown ( $E_{pit}$ ) is the point of abrupt change in voltage value after the curve enters the anodic zone, used to characterize the voltage at which the passivation state ends. In contrast, the Tafel segment of 500E shows a passivation stage, entering a breakdown state at  $-0.55$  V, with a subsequent decrease in current density. After 60 days passivation, for the polarization curves and impedance spectral changes, it can be seen that both materials exhibit greatly improved electrochemical stability, with increasing complexity in layer chemical composition and gradual changes in electrochemical activity. The open circuit potentials of both steels gradually shift towards more positive values, while the fluctuation in corrosion current density remains significant, stabilizing after 288 h and 576 h of corrosion.



**Table 3.** Parameters of original-state Tafel curves of two steel types.

Sample	Status	$E_{OCP}$ (V vs. SCE)	$E_{corr}$ (V vs. SCE)	$I_{corr}$ ( $A \cdot cm^{-2}$ )	$E_{pit}$ (V vs. SCE)	Corrosion Rate ( $mm \cdot A^{-1}$ )
500cE	Original	−0.6038	−0.6448	$2.2709 \times 10^{-6}$	−0.4821	0.0214
500E		−0.5950	−0.9012	$2.5482 \times 10^{-6}$	−0.4528	0.0226
500CE-60D	Passivation for 60 days	−0.4716	−0.5885	$8.5599 \times 10^{-6}$	−0.4048	0.0099
500E-60D		−0.5720	−0.6112	$1.2117 \times 10^{-5}$	−0.6112	0.0141
500CE-60D-1H	After passivation, corrosion occurs at different durations	−0.5549	−0.5872	$3.6441 \times 10^{-6}$	−0.5872	0.0424
500E-60D-1H		−0.6155	−0.6700	$5.6543 \times 10^{-6}$	−0.6700	0.0659
500CE-60D-6H		−0.5100	−0.4803	$1.2521 \times 10^{-6}$	−0.4594	0.0145
500E-60D-6H		−0.6192	−0.6757	$3.2552 \times 10^{-6}$	−0.6757	0.0379
500CE-60D-12H		−0.6235	−0.5357	$1.6044 \times 10^{-6}$	−0.5357	0.0312
500E-60D-12H		−0.6144	−0.8178	$2.7595 \times 10^{-5}$	−0.5668	0.3216
500CE-60D-24H		−0.5962	−0.5481	$5.872 \times 10^{-6}$	−0.5481	0.0673
500E-60D-24H		−0.6444	−0.8881	$3.0566 \times 10^{-5}$	−0.5668	0.3563
500CE-60D-72H		−0.6123	−0.5854	$0.1911 \times 10^{-6}$	−0.5854	0.2228
500E-60D-72H		−0.6837	−0.8944	$2.1347 \times 10^{-6}$	−0.8944	0.2843
500CE-60D-144H		−0.6031	−0.6891	$4.336 \times 10^{-6}$	−0.6891	0.0505
500E-60D-144H		−0.6438	−0.8481	$1.0673 \times 10^{-4}$	−0.5108	1.2441
500CE-60D-288H		−0.6067	−0.5771	$2.341 \times 10^{-5}$	−0.5771	0.3541
500E-60D-288H		−0.6846	−0.9149	$1.7568 \times 10^{-5}$	−0.6860	0.2047
500CE-60D-576H		−0.6181	−0.6073	$6.9163 \times 10^{-6}$	−0.6073	0.0806
500E-60D-576H		−0.6771	−0.9051	$6.5781 \times 10^5$	−0.6641	0.7667

As depicted in the Figure 4, both steels exhibit capacitive behavior in the Nyquist plots, characterized by semicircular arcs, indicating similar surface reactions and electrochemical characteristics in the chloride environment. The significant difference in the capacitive arc radius between the original states of 500CE and 500E indicates that the alloy-modified corrosion-resistant steel can effectively inhibit metal dissolution processes in chloride environments. To further analyze their corrosion resistance mechanisms, the Nyquist plots were fitted using software and equivalent circuit models, as mentioned earlier, with the fitting results shown in Table 4.

**Table 4.** Fitting results of electrochemical impedance spectra of two steels in original state.

Sample	Status	$R_s$ ( $\Omega \cdot cm^2$ )	$R_f$ ( $\Omega \cdot cm^2$ )	$Q_f$		$R_{ct}$ ( $\Omega \cdot cm^2$ )	$Q_{dl}$	
				$Y_0$ ( $\Omega^{-1} \cdot cm^{-2} \cdot s^n$ )	$n1$		$Y_0$ ( $\Omega^{-1} \cdot cm^{-2} \cdot s^n$ )	$n2$
500cE	Original	5.58	26.99	$52.07 \times 10^{-5}$	0.78	1287.71	$36.34 \times 10^{-5}$	0.39
500E		5.22	107.02	$44.25 \times 10^{-5}$	0.82	3.48	$46.63 \times 10^{-5}$	0.28
500CE-60D	Passivation for 60 days	4.30	30.32	$13.94 \times 10^{-5}$	0.85	2134.8	$12.72 \times 10^{-5}$	0.82
500E-60D		5.0169	18.20	$23.33 \times 10^{-5}$	0.81	1711.4	$15.43 \times 10^{-5}$	0.75
500CE-60D-1H	After passivation, corrosion occurs at different durations	4.8524	12.97	$56.47 \times 10^{-5}$	0.74	1438.4	$38.52 \times 10^{-5}$	0.87
500E-60D-1H		4.97	1.15	$3.24 \times 10^{-5}$	0.92	1516.3	$85.08 \times 10^{-5}$	0.73
500CE-60D-6H		5.72	20.77	$20.76 \times 10^{-5}$	0.84	1599.2	$12.42 \times 10^{-5}$	0.76
500E-60D-6H		6.56	1.42	$10.57 \times 10^{-5}$	0.62	1744.1	$18.79 \times 10^{-5}$	0.75
500CE-60D-12H		6.42	1.39	$1.07 \times 10^{-5}$	0.98	3239	$55.31 \times 10^{-5}$	0.73
500E-60D-12H		5.55	12.55	$109.83 \times 10^{-5}$	0.68	1103.8	$18.79 \times 10^{-6}$	0.65
500CE-60D-24H		4.89	26.95	$44 \times 10^{-5}$	0.80	1355	$1.91 \times 10^{-29}$	0.81
500E-60D-24H		7.71	13.01	$154.96 \times 10^{-5}$	0.74	1467.8	$156.54 \times 10^{-5}$	0.73
500CE-60D-72H		4.59	0.94	$21.4 \times 10^{-5}$	0.91	1685.6	$101.5 \times 10^{-5}$	0.71
500E-60D-72H		7.5002	1692.1	$297.96 \times 10^{-5}$	0.02	1131.3	$245.98 \times 10^{-5}$	0.47
500CE-60D-144H		5.88	1.06	$49 \times 10^{-5}$	0.94	1178.4	$76 \times 10^{-5}$	0.71
500E-60D-144H		5.97	2.42	$40.01 \times 10^{-5}$	0.84	839.4	$66.1 \times 10^{-4}$	0.65
500CE-60D-288H		5.70	1.29	$10.2 \times 10^{-5}$	0.82	1658.3	$46.77 \times 10^{-5}$	0.78
500E-60D-288H		7.62	400.33	$199.71 \times 10^{-5}$	0.71	1314.2	$245.9 \times 10^{-5}$	0.45
500CE-60D-576H		7.0577	1.9435	$18.62 \times 10^{-5}$	0.80	1799.8	$38.36 \times 10^{-5}$	0.78
500E-60D-576H		6.05	1.87	$48.9 \times 10^{-5}$	0.90	1774.8	$113.6 \times 10^{-5}$	0.75

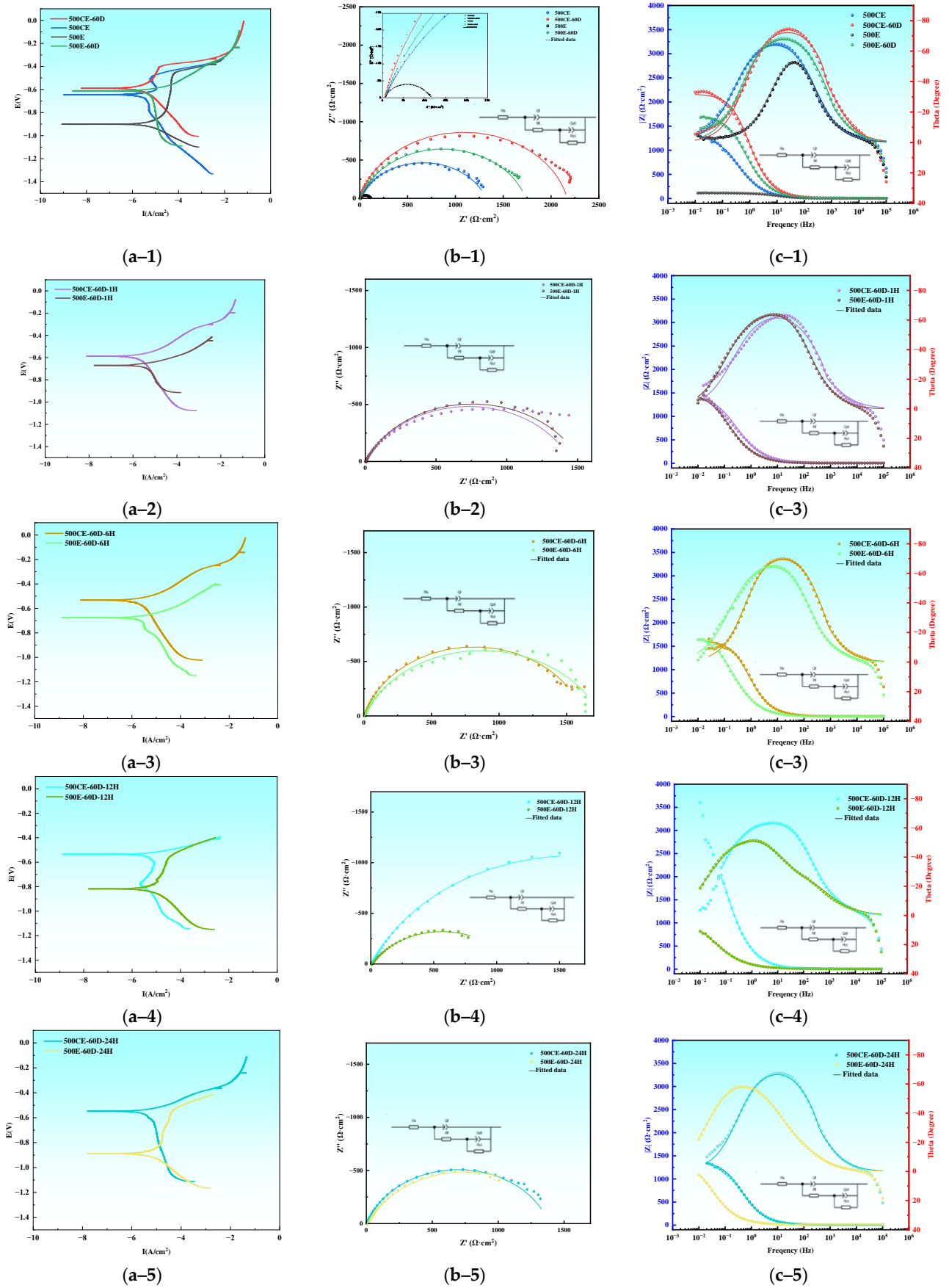
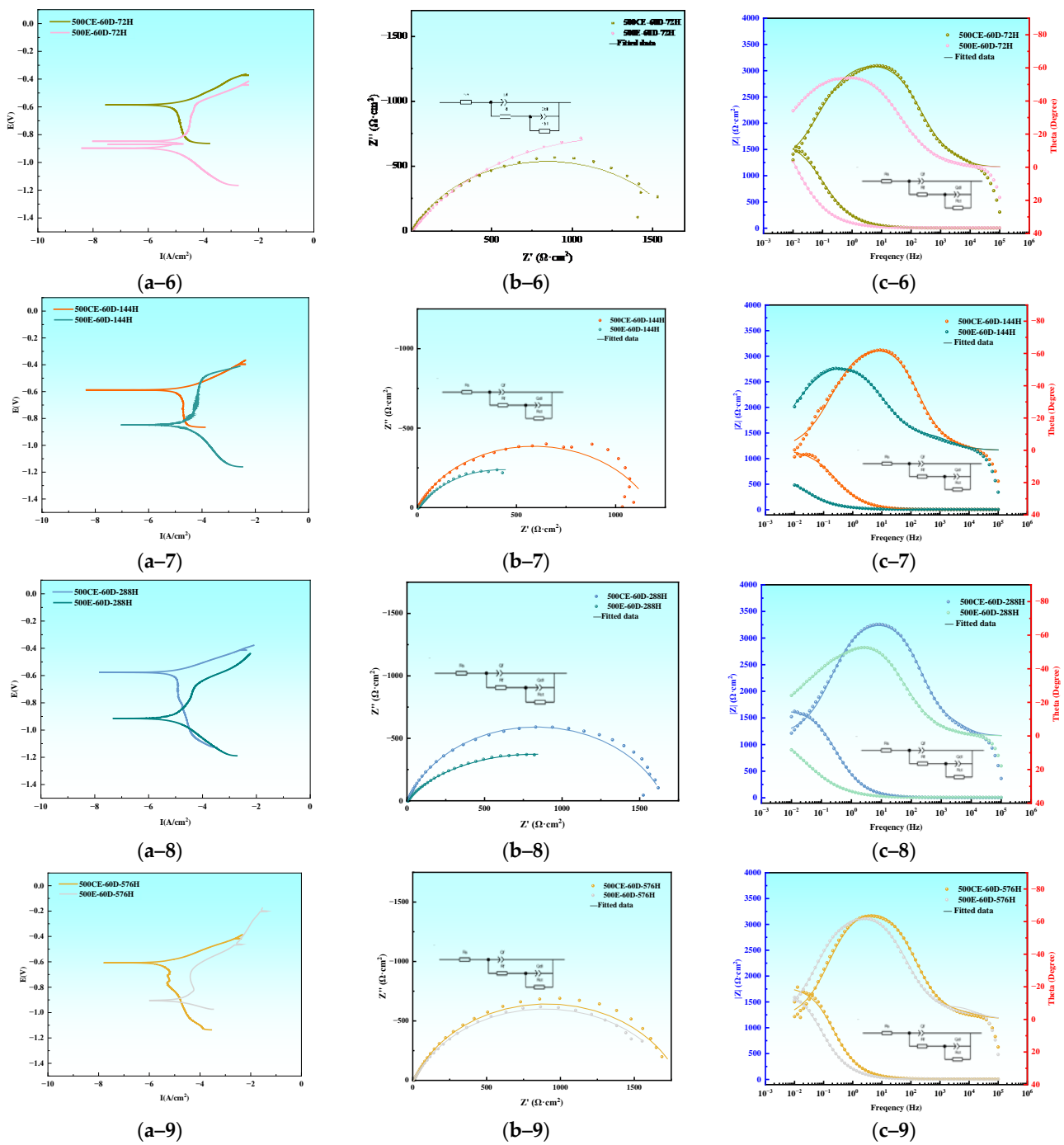


Figure 4. Cont.



**Figure 4.** Atomic force microscopy height maps and three-dimensional morphology of experimental steel reinforcement microstructures, along with local potential variations in corresponding regions: (a-1-a-9) Tafel plot; (b-1-b-9) Nyquist plot; (c-1-c-9) Bode plot.

After 60 days passivation, the impedance of 500CE reaches its maximum, with the capacitive arc radius of the low-alloy corrosion-resistant steel significantly larger than that of ordinary carbon steel. From the Bode plot, it is evident that in the high-frequency range, both exhibit nearly identical impedance values without significant fluctuations. As corrosion progresses, within the frequency range of  $10^{-3}$  to  $10^3$  Hz, 500CE shows a greater increase in impedance magnitude with decreasing frequency, whereas 500E exhibits a more gradual change in impedance and a decreasing trend near  $10^{-2}$  Hz. Based on the fitting parameters, there is a difference in polarization resistance between the two, indicating weaker charge transfer ability during corrosion. This demonstrates that alkaline passivation

significantly enhances the corrosion resistance of 500CE after 60 days, highlighting its excellent resistance to 2 wt.% chloride corrosion in early service stages.

From the corrosion of 72 h to that of 576 h, 500CE and 500E both show characteristic impedance behavior, with a reduction in capacitive features and a Nyquist plot displaying a monotonic increasing trend. 500CE and 500E both show a decreasing and increasing trend of  $R_{ct}$  during the corrosion process from 72 h to 576 h, with the former having an  $R_{ct}$  of 1685.6 ohm and the latter having an  $R_{ct}$  of 1131.1 ohm after 72 h of corrosion. With the extension of corrosion time,  $R_{ct}$  reaches a minimum value after 144 h corrosion, with 500CE decaying at 507.2 ohm and 500E decaying at 291.9 ohm, and  $R_{ct}$  continues to increase in the subsequent corrosion process, with both eventually stabilizing at around 1800 ohm. At this stage, the difference in impedance arc radius between 500CE and 500E diminishes, but 500CE still maintains a larger arc radius than 500E, as observed from the Bode plot. This similarity in frequency response and impedance variation indicates that their sensitivity to disturbances at different frequencies during corrosion days is not significantly different. The fitting parameters further confirm that both experimental steels are less prone to corrosion on their surfaces, exhibiting relatively poor electrochemical activity.

In conclusion, the corrosion resistance of the low-alloy corrosion-resistant steel 500CE remains superior to that of 500E in the later stages of corrosion. 500CE shows more stable electrochemical activity and superior corrosion resistance under service conditions, particularly in a passivated state. However, the duration of passivation does not directly correlate with corrosion resistance performance. While the impedance arc radius reaches its maximum after 60 days of passivation, the membrane resistance peaks after 576 h corrosion. As the corrosion cycle progresses, both the impedance arc radius and polarization resistance decrease, highlighting that the corrosion resistance of the low-alloy corrosion-resistant steel is better in the early stages of service.

### 3.4. XPS Analysis of Outer Layer

Figure 5 presents the XPS spectra of the outermost corrosion products of both steel types after various durations of passivation given that alloying elements predominantly accumulate in the inner layer during the advanced stages of corrosion, which significantly influences the progress of corrosion. The discussion is summarized below.

As Equations (1)–(3) show, in the anode area, metal atoms are oxidized into ions, moving out of the lattice array and into the solution; in the cathode area of the atmospheric oxygen diffusion, they move to the vicinity of the rebar and are dissolved in the water film on the surface of the rebar, by which it absorbs the electrons coming from the anode to reduce the reaction so that the cathode can depolarize. The cathode area on the surface of the rebar and the anode area form a closed connected electrical circuit system; the corrosion reaction of the rebar generated  $Fe^{2+}$  and  $OH^-$  combined to form insoluble  $Fe(OH)_2$ , which came into contact with oxygen to stimulate further oxidation ( $Fe(OH)_3$ ). Due to the oxidation,  $Fe(OH)_2$  is not fully oxidized; after drying to produce  $Fe_3O_4$ ,  $Fe(OH)_3$  is dehydrated to produce  $Fe_2O_3$ .



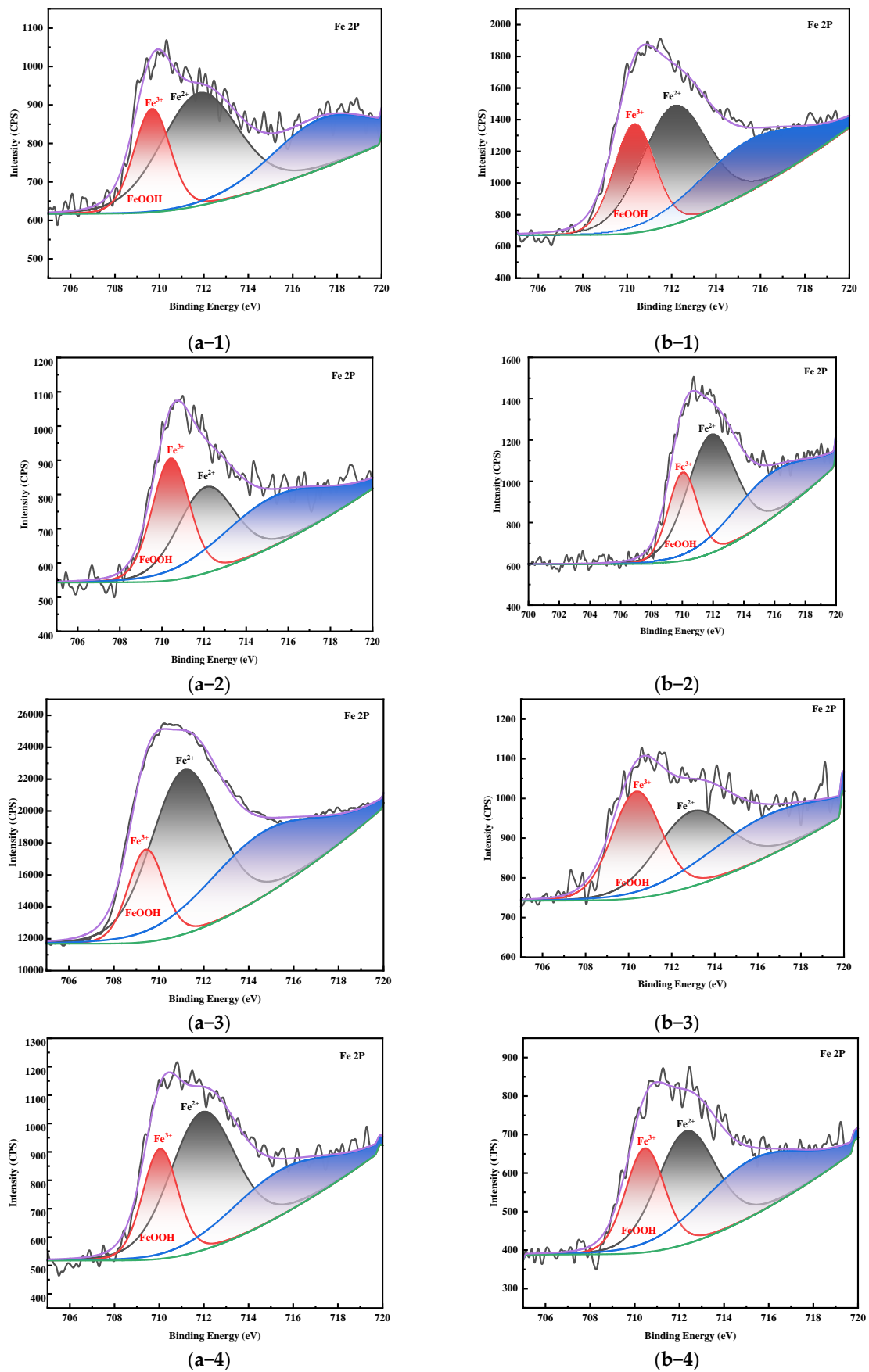
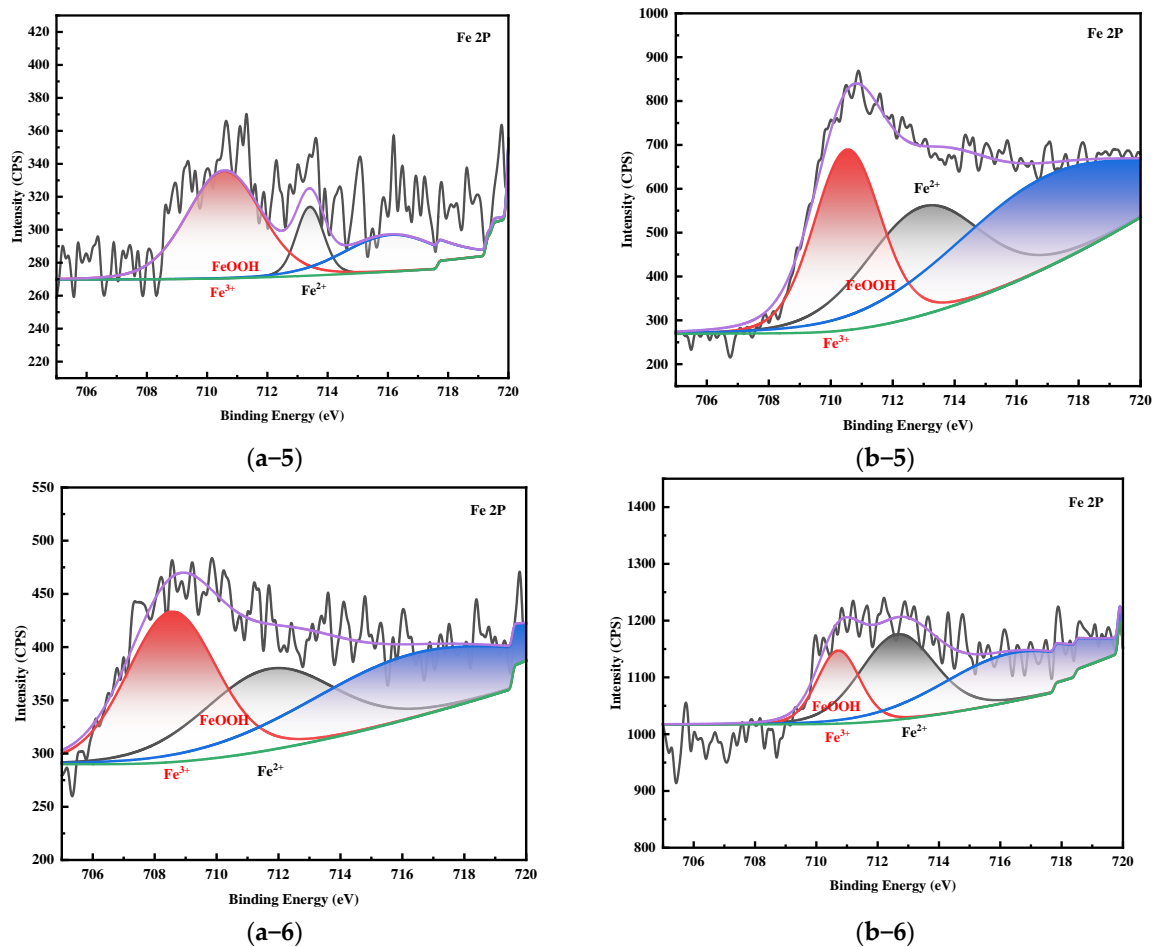


Figure 5. Cont.



**Figure 5.** Fe 2p XPS spectra of inner layers after 60 days of passivation in different corrosion environments for two types of steels: (a-1) 500CE-60D-12H; (a-2) 500CE-60D-24H; (a-3) 500CE-60D-72H; (a-4) 500CE-60D-144H; (a-5) 500CE-60D-288H; (a-6) 500CE-60D-576H; (b-1) 500E-60D-12H; (b-2) 500E-60D-24H; (b-3) 500E-60D-72H; (b-4) 500E-60D-144H; (b-5) 500E-60D-288H; (b-6) 500E-60D-576H.

As the corrosion duration increases, the  $\text{Fe}^{2+}$  content in the outer layer of 500CE shows an initial increase followed by stabilization, indicating that in the early stages of corrosion, the main components of the outer layer are FeO, partially oxidized  $\text{Fe}_3\text{O}_4$ , and a small amount of FeOOH. FeOOH is hydroxyl iron oxide; in the early stage of corrosion, its generation time is earlier than that of  $\text{Fe}_3\text{O}_4$ , and FeOOH has a variety of notification isomers, such as  $\alpha$ -FeOOH,  $\beta$ -FeOOH, and  $\gamma$ -FeOOH, which are the main components of the passivation film on the surface of the steel. The corrosion of chlorine salts presents a certain impediment to the role of the  $\alpha$ -FeOOH organization structure, i.e., to its most dense and the most stable electrical and chemical properties.  $\text{Fe}_3\text{O}_4$  is the intermediate product of the transition from local corrosion to the uniform corrosion stage of the steel bar, mainly  $\text{Fe}^{2+}$  and  $\text{Fe}^{3+}$  combined with oxygen ions, which is chemically unstable, with further corrosion conditions. And in the corrosion process, the volume of hydroxyl iron oxide is smaller than that of iron tetraoxide, and the corrosion expansion process of the rust layer expansion has an inhibitory effect.

Peaking at 72 h of corrosion, from 144 h to 576 h of corrosion, stable  $\text{Fe}^{3+}$  gradually enriches on the surface, and the intensity of the  $\text{Fe}^{3+}$  peaks does not show significant decay, indicating that the  $\text{Fe}_2\text{O}_3$  formed on the surface of 500CE is relatively stable and dense, i.e., capable of being retained during the corrosion process. In contrast, for 500E, as the corrosion progresses, the intensity of the  $\text{Fe}^{2+}$  peaks gradually decreases, indicating that the oxidation reaction is more intense compared to 500CE.  $\text{Fe}_3\text{O}_4$  and FeOOH on the surface of

the layer continuously transform into  $\text{Fe}_2\text{O}_3$ , indicating that the outer layer surface of 500E is relatively porous.

#### 4. Conclusions

This study leveraged microalloying technology to prepare 500 Mpa grade rebar with the goal of reducing the surface electrochemical activity of high-strength corrosion-resistant rebars in service conditions and enhancing their corrosion resistance. This research conducted comparative analyses of chemical compositions, microstructures, and potential differences, along with experiments on polarization curves, impedance spectra, and the evolution of iron ion states in external layers. The findings of this study are intended to deepen further our understanding of the corrosion behavior and underlying mechanisms of corrosion resistance in service conditions. The research findings are as follows:

(1) Microscopic observation and SKPM detection under identical corrosion conditions reveal distinct differences between 500CE and 500E steels. The 500CE steel, regulated by alloying elements, exhibits finer ferrite grains and a notably lower pearlite content compared to 500E steel. This microstructural composition contributes to a more uniform corrosion process, reducing the risk of catastrophic corrosion failure. The microstructure of 500CE affords it its potential to stabilize at a more positive electrical potential without significant contrasts due to structural differences. Conversely, 500E displays larger grain sizes in its microstructure, with alternating surface potentials relative to the probe and significant absolute potential fluctuations, which may lead to intergranular corrosion. However, its microstructural uniformity and electrochemical activity remain stable.

(2) The low-alloy corrosion-resistant steel 500CE has been proven to exhibit superior corrosion resistance in the later stages of corrosion when compared to 500E. Even under conditions of prolonged passivation, 500CE maintains more stable electrochemical activity and demonstrates a higher degree of corrosion resistance. However, the passivation duration does not show a direct linear relationship with its corrosion resistance capabilities. While the impedance arc radius of 500CE attains its maximum extent after 60 days of passivation, the film resistance is found to peak at 576 h into the corrosion process. As the corrosion progresses, both the impedance arc radius and the polarization resistance are observed to diminish. This trend suggests that the low-alloy corrosion-resistant steel shows enhanced resistance in the initial stages of corrosion.

(3) In the early stages of the corrosion of 500CE, the main components of the external layer are FeO, partially oxidized  $\text{Fe}_3\text{O}_4$ , and small amounts of FeOOH. In the later stages of corrosion,  $\text{Fe}^{3+}$  is gradually enriched on the surface, indicating that the  $\text{Fe}_2\text{O}_3$  formed on the surface of the 500CE layer is relatively stable and dense, capable of persisting during the corrosion process. In contrast, as corrosion progresses in 500E, the intensity of the  $\text{Fe}^{2+}$  peak gradually decreases, suggesting that its oxidation reactions are more severe compared to those of 500CE.

Furthermore, this study thoroughly investigates the 2 wt.% chloride corrosion behavior of low-alloy corrosion-resistant steel reinforcement under service conditions, providing a theoretical basis and practical guidance for extending the service life of reinforced concrete structures.

**Author Contributions:** Conceptualization, J.Y. and P.L.; methodology, J.Y. and P.L.; software, J.Y. and P.L.; validation, J.Y. and P.L.; formal analysis, J.Y. and P.L.; investigation, J.Y. and P.L.; resources, S.Y. and H.Z.; data curation, S.Y. and J.Y.; writing—original draft preparation, J.Y. and M.X.; writing—review and editing, J.Y. and S.Y.; visualization, J.Y.; supervision, S.Y.; project administration, J.Y. and P.L. All authors have read and agreed to the published version of the manuscript.

**Funding:** This research received no external funding.

**Institutional Review Board Statement:** Not applicable.

**Informed Consent Statement:** Not applicable.

**Data Availability Statement:** The original contributions presented in the study are included in the article, further inquiries can be directed to the corresponding author.

**Conflicts of Interest:** Author Jing Yuan was employed by the company Xinyu Iron & Steel Group Co., Ltd. The remaining authors declare that the research was conducted in the absence of any commercial or financial relationships that could be construed as a potential conflict of interest.

## References

1. Hou, L.; Li, W.; Zheng, H.; Ji, T.; Tian, H. Research Progress on Corrosion Protection Technology for Marine Reinforced Concrete Structures. *Mater. Prot.* **2017**, *50*, 62–67. [\[CrossRef\]](#)
2. Wang, B.; Jin, Q.; Du, X.; Wang, C.; Li, G.; Zheng, Y.; Sun, H.; Zhang, D.; Ma, C. Corrosion mechanism and microstructure evolution of yttrium-doped marine steel. *J. Mater. Res. Technol.* **2024**, *28*, 2752–2766. [\[CrossRef\]](#)
3. Wen, Y.; Ma, X.; Cai, Y.; Liu, L.; Zhou, L.; Liu, Q.-F. Corrosion inhibition mechanism of vitamins on steel bars in chloride environments: Experimental analysis and quantum chemical calculation. *Constr. Build. Mater.* **2023**, *406*, 133424. [\[CrossRef\]](#)
4. Chen, M.; Yuan, H.; Qin, X.; Wang, Y.; Zheng, H.; Yu, L.; Cai, Y.; Liu, Q.-F.; Liu, G.; Li, W. Improve corrosion resistance of steel bars in simulated concrete pore solution by the addition of EDTA intercalated CaAl-LDH. *Corros. Sci.* **2024**, *226*, 111636. [\[CrossRef\]](#)
5. Ouarga, A.; Zirari, T.; Fashu, S.; Lahcini, M.; Ben Youcef, H.; Trabadelo, V. Corrosion of iron and nickel based alloys in sulphuric acid: Challenges and prevention strategies. *J. Mater. Res. Technol.* **2023**, *26*, 5105–5125. [\[CrossRef\]](#)
6. Gao, J.; Xu, Q.; Yang, S.; Li, C.; Li, X.; Zhang, X. Interfacial corrosion behaviors of coating/Q450NQR1 weathering steel under simulated harsh marine atmosphere. *J. Mater. Res. Technol.* **2022**, *21*, 2471–2480. [\[CrossRef\]](#)
7. Farag, Z.R.; Moustapha, M.E.; Anouar, E.H.; Abd El-Hafeez, G.M. The inhibition tendencies of novel hydrazide derivatives on the corrosion behavior of mild steel in hydrochloric acid solution. *J. Mater. Res. Technol.* **2022**, *16*, 1422–1434. [\[CrossRef\]](#)
8. Less, T.; Demir, A.; Sezen, H. Structural performance and corrosion resistance of fiber reinforced polymer wrapped steel reinforcing bars. *Constr. Build. Mater.* **2023**, *366*, 130176. [\[CrossRef\]](#)
9. Luo, D.; Li, Y.; Lim, K.-S.; Yang, H.; Ahmad, H. Development of Fe-C film coated polymer optical fiber sensor for steel bar corrosion monitoring. *Measurement* **2023**, *210*, 112561. [\[CrossRef\]](#)
10. Liu, L.; Zhang, H.; Bi, H.; Chang, E.; Li, M. Corrosion behavior of cold-rolled metastable Cr–Mn–Ni–N austenitic stainless steel in acidic NaCl solution. *J. Mater. Res. Technol.* **2022**, *19*, 278–288. [\[CrossRef\]](#)
11. Zhang, Y.; Yuan, R.; Yang, J.; Xiao, D.; Luo, D.; Zhou, W.; Tuo, C.; Wu, H.; Niu, G. Effect of tempering on corrosion behavior and mechanism of low alloy steel in wet atmosphere. *J. Mater. Res. Technol.* **2022**, *20*, 4077–4096. [\[CrossRef\]](#)
12. Bui, H.T.; Maekawa, K.; Tan, K.H. Microcell and macrocell corrosion of steel bars in reinforced concrete slabs under different corrosive environments and cathode/anode configurations. *Cem. Concr. Compos.* **2023**, *138*, 104989. [\[CrossRef\]](#)
13. Pan, D.; Niu, D.; Li, Z. Corrosion products of low-alloy steel bars and their induction of cracking in seawater sea-sand concrete cover. *Constr. Build. Mater.* **2023**, *389*, 131800. [\[CrossRef\]](#)
14. Hameed, R.S.A.; Obeidat, S.; Qureshi, M.T.; Al-Mhyawi, S.R.; Aljuhani, E.H.; Abdallah, M. Silver nanoparticles—Expired medicinal drugs waste accumulated at hail city for the local manufacturing of green corrosion inhibitor system for steel in acidic environment. *J. Mater. Res. Technol.* **2022**, *21*, 2743–2756. [\[CrossRef\]](#)
15. Jin, Z.-H.; Jiang, C.; Gu, X.-L.; Dong, Z. Macro-cell corrosion between crossed steel bars in cracked concrete. *Constr. Build. Mater.* **2022**, *350*, 128867. [\[CrossRef\]](#)
16. Luo, B.; Hu, Q.; Liu, J.; Huang, F. Effect of crevice gap on crevice corrosion initiation and development of 2205 duplex stainless steel in NaCl solution. *J. Mater. Res. Technol.* **2022**, *21*, 2584–2597. [\[CrossRef\]](#)
17. Chauhan, S.; Muthulingam, S. Fatigue life estimation of TMT reinforcing steel bar considering pitting corrosion and high temperature impacted surface topography. *Int. J. Fatigue* **2023**, *175*, 107810. [\[CrossRef\]](#)
18. Kanwal, M.; Khushnood, R.A.; Adnan, F.; Wattoo, A.G.; Jalil, A. Assessment of the MICP potential and corrosion inhibition of steel bars by biofilm forming bacteria in corrosive environment. *Cem. Concr. Compos.* **2023**, *137*, 104937. [\[CrossRef\]](#)
19. Morshed-Behbahani, K.; Zakerin, N. A review on the role of surface nanocrystallization in corrosion of stainless steel. *J. Mater. Res. Technol.* **2022**, *19*, 1120–1147. [\[CrossRef\]](#)
20. Zhu, W.; Ren, Y.; Yu, Z.; Tang, F.; Xu, Y.; Xu, Y. Characteristics of the non-uniform corrosion of the steel bars extracted from the marine transportation infrastructures. *J. Build. Eng.* **2024**, *87*, 109108. [\[CrossRef\]](#)
21. Zhang, F.; Myers, J.J.; Liao, W.; Hui, C.; Ma, H. Investigation of corrosion mechanism of ribbed mild steel bars coated with magnesium potassium phosphate cement paste. *Constr. Build. Mater.* **2023**, *371*, 130639. [\[CrossRef\]](#)
22. Wang, Y.; Ren, J.; Zuo, J.; Du, H.; Zhu, C.; Zhang, Y.X.; Ren, Y.; Chen, Y. Corrosion protection of steel bar enabled by monofluorophosphate-bearing composites with sustained-release capability. *J. Build. Eng.* **2023**, *80*, 108087. [\[CrossRef\]](#)
23. Santos Martinez, J.D.; Ladino, D.H.; Calderón Hernández, J.W.; Falleiros, N.A.; de Melo, H.G. Corrosion characterization of new low manganese microalloyed X65 steels in sour and NON-SOUR synthetic seawater. *J. Mater. Res. Technol.* **2022**, *18*, 3198–3214. [\[CrossRef\]](#)
24. Wang, F.; Xue, X.; Hua, J.; Chen, Z.; Huang, L.; Wang, N.; Jin, J. Non-uniform corrosion influences on mechanical performances of stainless-clad bimetallic steel bars. *Mar. Struct.* **2022**, *86*, 103276. [\[CrossRef\]](#)



25. Xin, Y.; Song, K.; Li, Y.; Fan, E.; Lv, X. Environmentally assisted stress corrosion cracking behaviour of low alloy steel in SO<sub>2</sub>-containing NaCl solution. *J. Mater. Res. Technol.* **2022**, *19*, 3255–3271. [[CrossRef](#)]
26. Bai, S.-B.; Chen, Y.-A.; Liu, X.; Lu, H.-H.; Bai, P.-K.; Li, D.-Z.; Huang, Z.-Q.; Li, J.-Y. Research status and development prospect of Fe–Mn–C–Al system low-density steels. *J. Mater. Res. Technol.* **2023**, *25*, 1537–1559. [[CrossRef](#)]
27. Zhao, L.; Wang, J.; Gao, P.; Yuan, Y. Experimental study on the corrosion characteristics of steel bars in concrete considering the effects of multiple factors. *Case Stud. Constr. Mater.* **2024**, *20*, e02706. [[CrossRef](#)]
28. Naderi, R.; Bautista, A.; Shagñay, S.; Velasco, F. Licorice (*Glycyrrhiza glabra*) as corrosion inhibitor of carbon steel reinforcing bars in mortar and its synergic effect with nitrite. *J. Ind. Eng. Chem.* **2024**, *129*, 620–633. [[CrossRef](#)]
29. Yu, X.; Yan, Z.; Li, J. Comprehensive study on corrosion induced structural deterioration of steel bars in reinforced concrete beams. *J. Constr. Steel Res.* **2024**, *214*, 108504. [[CrossRef](#)]
30. Cui, L.; Hang, M.; Huang, H.; Gao, X. Experimental study on multi-component corrosion inhibitor for steel bar in chloride environment. *Constr. Build. Mater.* **2021**, *313*, 125533. [[CrossRef](#)]
31. Wang, Z.; Zhang, X.; Cheng, L.; Liu, J.; Wu, K. Role of inclusion and microstructure on corrosion initiation and propagation of weathering steels in marine environment. *J. Mater. Res. Technol.* **2021**, *10*, 306–321. [[CrossRef](#)]
32. Wang, L.; Li, Y.; Mei, K.; Chen, M.; Liu, J. Evaluation of combined addition of nitrite and chloride on the corrosion behavior of steel bars in modified magnesium oxysulfate cement paste. *Constr. Build. Mater.* **2024**, *422*, 135794. [[CrossRef](#)]
33. Anaman, S.Y.; Zhang, S.; Lee, J.-S.; Cho, H.-H.; Hong, S.-T. A comprehensive assessment of the galvanic corrosion behavior of an electrically assisted pressure joint of dissimilar stainless steel alloys under uniaxial tensile stress. *J. Mater. Res. Technol.* **2022**, *19*, 3110–3129. [[CrossRef](#)]
34. Zhang, S.; Liu, J.; Tang, M.; Zhang, X.; Wu, K. Role of rare earth elements on the improvement of corrosion resistance of micro-alloyed steels in 3.5 wt.% NaCl solution. *J. Mater. Res. Technol.* **2021**, *11*, 519–534. [[CrossRef](#)]

**Disclaimer/Publisher’s Note:** The statements, opinions and data contained in all publications are solely those of the individual author(s) and contributor(s) and not of MDPI and/or the editor(s). MDPI and/or the editor(s) disclaim responsibility for any injury to people or property resulting from any ideas, methods, instructions or products referred to in the content.